Physica A 629 (2023) 129163

Contents lists available at ScienceDirect

Physica A

journal homepage: www.elsevier.com/locate/physa

Revealing traits of phytopathogenic status induced by *Xylella Fastidiosa* in olive trees by analysing multifractal and informational patterns of MODIS satellite evapotranspiration data

Luciano Telesca [a,*], Nicodemo Abate [b], Farid Faridani [c], Michele Lovallo [d], Rosa Lasaponara [a]

[a] *Institute of Methodologies for Environmental Analysis, National Research Council, C.da S.Loja, Tito, 85050, Italy*
[b] *Institute of Heritage Science, National Research Council, C.da S.Loja, Tito, 85050, Italy*
[c] *Department of European and Mediterranean Cultures, Environment, and Cultural Heritage, University of Basilicata, Potenza, 85100, Italy*
[d] *Agenzia Regionale per la Protezione dell'Ambiente della Basilicata, Potenza, 85100, Italy*

ARTICLE INFO

Article history:
Received 16 April 2023
Received in revised form 21 July 2023
Available online 9 September 2023

Keywords:
Satellite data
Vegetation
Xylella Fastidiosa
Fisher–Shannon analysis
Multifractal detrended fluctuation analysis

ABSTRACT

In this work the time variability of MODIS satellite evapotranspiration data was investigated by using the informational Fisher–Shannon analysis and the multifractal detrended fluctuation analysis to reveal the presence of *Xylella Fastidiosa* in olive trees, a very dangerous phytobacterium capable to induce a severe disease in olive trees, known as olive quick decline syndrome. Several hundred pixels of infected and healthy sites located in southeastern Italy were analysed. Our results suggest that the informational (Fisher Information Measure and Shannon entropy) and multifractal (h_q-range, multifractal width W and maximum α_0) parameters allow a good discrimination between infected and healthy sites, envisaging the use of the combination of this two methods as an operational tool for early diagnosis of plant deterioration due to the bacterium.

1. Introduction

The biodiversity reorganization and shift of species distribution, due to the fast time evolution of climate change [1], along with the increase of global connections around the world, has represented one of the major drivers of biological invasions causing a great environmental problem [2]. In fact, the environmental changes as consequence of the climate change and the disruption of the local communities after biological invasions have altered the plant–vector–pathogen interactions [3] favouring the onset of extremely dangerous phytopathogens. *Xylella Fastidiosa* is certainly one of these. It is transmitted by several vectors, like the *Homalodisca vitripennis*, a sap-sucking leafhopper that comprises 18 species, native to southeastern United States and northeastern Mexico [4]. *Xylella Fastidiosa* is the cause of important economic loss due to several plant infections, like the Pierce's disease of grapevines [5], the olive quick decline [6], the bacterial leaf scorch [7], the phony peach disease [8]. In Europe *Xylella Fastidiosa* was first detected in Italy in 2013 [9], and then in several other European countries; however this bacterium was also detected in the Middle East [10] and Asia [11],

* Corresponding author.
E-mail address: luciano.telesca@imaa.cnr.it (L. Telesca).

https://doi.org/10.1016/j.physa.2023.129163

being considered now a serious threat to large variety of plants of economic relevance and to forests becoming a real phytosanitary emergency [12].

Before 2013, only Krugner et al. [13] studied *Xylella Fastidiosa* subsp. *multiplex* detected in olive trees with leaf scorch and branch dieback; but in their experiments, consisting in recovering isolates from symptomatic trees and inoculating and vector-transmitting them to olive plants of different cultivars, infections did not cause the same symptoms observed in the field. Only after *Xylella Fastidiosa* was detected in olive orchards in southern Italy more deep investigation was performed on olive crop in Argentina and Brazil, where, symptomatic plants were also discovered to host *Xylella Fastidiosa* subsp. *pauca* [14,15], which is the same subspecies infecting the Italian olive trees [16]. Strona et al. [17] found that the factors contributing to the anchoring of *Xylella Fastidiosa* in the Apulia (southern Italy) were the wide distribution of olive groves in this territory and the large amount of *Philaenus spumarius L.* that is vector of this bacterium. A few studies have been focused on the precautionary prediction of risk areas for early detection in order to minimize damage [18] and determine the potential distribution of *Xylella Fastidiosa* to establish basic data for monitoring and controlling its infection [19].

Up to now, no treatment has been found to let the infected trees to recover, and only plucking the infected trees has been proposed as an effective means to obstacle the diffusion of the epidemy. Of course, an early identification of asymptomatic or infected plants with visible symptoms of desiccation would represent a much more efficient disease management strategy, lowering the risk of spreading of infection. At present the most commonly used approach is the visual inspection that has some advantages, like rapidity, easiness and cost-effectiveness; but, the variability in accuracy due to the subjective assessment of the level of the symptoms could make the assessment of the disease not a standard process. Furthermore, the collected samples have to be analysed in the laboratory, and this make visual inspection time-consuming, expensive and destructive [20].

Over the years, Remote Sensing (RS) technologies have been gaining special attention in the monitoring of vegetation changes and dynamics and more recently in the detection of plant diseases and pests. Remote sensing methods can capture the degradation signs induced by many pathogen infections. In fact, multi-temporal and multi-spectral satellite data can identify the signals induced by the reduced chlorophyll pigment content and in turn photosynthetic activity, monitoring the nutritional, physiological and water status of plants; factors that can give crucial information on the health status of the plant, and, in turn, on the possible ongoing infection.

Castrignanó et al. [21] explored the use of Unmanned Aerial Vehicle (UAV) in combination with a multispectral radiometer for early detection of *Xylella Fastidiosa* infection. By mean of four drone flying over three olive groves in Apulia (southern Italy) from 2017 to 2019, they classified the severity of the infection in olive trees at an early stage, combining geostatistics and discriminant analysis, obtaining promising results that encourage the application of UAV technology for the early detection of *Xylella Fastidiosa* infection. Zarco-Tejada et al. [22] showed that *Xylella Fastidiosa* infection can be revealed in olive trees before symptoms appear, by analysing the changes in plant functional traits retrieved from airborne imaging spectroscopy and thermography. Camino et al. [23] coupled a spatial spread model with the probability of *Xylella Fastidiosa* infection predicted by a RS-driven support vector machine model, predicting accurately plant disease spatial distribution.

Since 2013, *Xylella Fastidiosa* has strongly impacted olive orchards in Apulia (souther Italy) inducing strong disease (known as olive quick decline syndrome) characterized by rapid branch desiccation and tree death. The bacterium multiplies in the conducting vessels of the xylem of the host plants, so that it obstructs the vessels that carry water and nutrients from the roots to the stem and up to the leaves, creating a sort of gel which prevents the regular flow of the fluid; as a consequence infected plants dry up completely [24].

Due to the mechanism of infection by *Xylella Fastidiosa*, the analysis of time series of evapotranspiration data to monitor the water status of plants seem suited to indicate the presence of this plant disease.

In particular, we investigated the time dynamics of several hundred pixels covering infected and healthy areas of southern Italy of MODIS-based evapotranspiration (ET) data, by means of two methods: the Fisher–Shannon analysis [25–28] and the multifractal detrended fluctuation analysis (MFDFA) [29,30], which are able to evidence the informational and the multiscaling properties of a time series, respectively, and to disclose complex patterns in signals as those characterizing the data investigated in this study. Both methods have been widely used in several research fields, from brain research [31] to biology [28,30,32] to econophysics [27,33] to geophysics [34,35]. Both methods have already been used to investigate complex dynamics in observational time series. da Silva et al. [36] applied the informational approach of the Fisher–Shannon method to study the time series of Standardized Precipitation Index (SPI) derived from monthly rainfall data at 133 gauging stations in Northeast (NE) Brazil distinguishing between different climatic regimes. Guignard et al. [37] found that the order/disorder features of high-frequency wind speed measured in urban layouts depends on height. Tripaldi et al. [38,39] distinguished different volcanic states by investigating the informational properties of geochemical and geodetic variables at Campi Flegrei (Italy). The multifractality has been utilized to discriminate different time dynamics between fire-affected and fire-unaffected sites by using MODIS Aqua and Terra satellite time series of normalized difference vegetation index and enhanced vegetation index [40], or to capture heart-failure signatures in heartbeat interval series [41].

2. Data

The analysed ET time series were obtained from the Moderate Resolution Imaging Spectroradiometer (MODIS). Each time series is 575 samples long and span from January 2010 to June 2022. These products, known as MOD16A2.006 (additional info at http://www.ntsg.umt.edu/project/modis/mod16.php) are free available online (https://lpdaac.usgs.gov) and in the Google Earth Engine (GEE) cloud database. For the purpose of our investigation the data were accessed from GEE, because cloud-based computing systems provides both updated MOD16A2.006 products ready-to-use and impressive computing power without the need to download and locally store these large amounts of products, thus strongly facilitating the use of big and open satellite data. The MOD16 dataset is made up of different variables (global evapotranspiration (ET), actual evapotranspiration (AET), latent heat flux (LE), potential ET (PET), potential LE (PLE)) regularly computed at 8-day, monthly and annual time scale intervals. MOD16 is a VI model based on the Penman–Monteith equation driven by MODIS data, and global meteorological reanalysis from the Modern-Era Retrospective analysis for Research and Applications (MERRA) [42]. ET can be estimated summing up soil evaporation (E_s), canopy evaporation (E_c), and canopy transpiration (T_c):

$$ET = Es + Ec + Tc \tag{1}$$

The radiation arriving to the soil can be partitioned between canopy and soil surface using the fraction of photosynthetically active radiation (f_{PAR}) assuming that f_{PAR} and canopy cover (f_c) are equal. MOD16 also considers the pixel wet surface fraction (f_w), calculated as a function of relative humidity (RH; when RH is higher than 70%, $f_w = RH4$), representing the fraction of vegetation and soil covered by water [43]. Estimations of E_s, E_c and T_c are given by the following equations:

$$E_s = f_w \frac{\Delta A_S + \frac{(1-f_c)\rho_a C_P (e_S - e_a)}{r_a^S}}{\Delta + \gamma \frac{r_S^S}{r_a^S}} + RH^{\frac{(e_S - e_a)}{\beta_{sm}}} (1 - f_W) \frac{\Delta A_S + \frac{(1-f_c)\rho_a C_P (e_S - e_a)}{r_a^S}}{\Delta + \gamma \frac{r_S^S}{r_a^S}} \tag{2}$$

$$E_c = f_w \frac{\Delta A_S + \frac{f_c \rho_a C_P (e_S - e_a)}{r_a^{wc}}}{\Delta + \gamma \frac{r_S^{wc}}{r_a^S}} \tag{3}$$

$$T_c = (1 - f_w) \frac{\Delta A_C + \frac{f_c \rho_a C_P (e_S - e_a)}{r_a^t}}{\Delta + \gamma (1 + \frac{r_S^t}{r_a^S})} \tag{4}$$

where Δ is the gradient of the saturation vapour pressure–temperature, Cp is the specific heat capacity, e_a and e_s are actual and saturated vapour pressure, respectively, ρ_a is the air density, A_s and A_c are the available energy to the soil and canopy, respectively, γ is the psychrometric constant, β_{sm} is a parameter related to the soil moisture constraint, r_s^s and r_a^s are the surface and aerodynamic resistance for the soil surface, r_s^{wc} and r_a^{wc} are the surface and aerodynamic resistance for the wet canopy evaporation and r_s^t and r_a^t are the surface and aerodynamic resistance for the canopy transpiration [43].

3. Selection of study areas

In October 2013, *Xylella Fastidiosa* was detected for the first time in the European Union on olive trees near Gallipoli in the Lecce province (Apulia, southern Italy). Since then, controls were in place to prevent the bacterium from spreading; nevertheless, *Xylella Fastidiosa* epidemy is continuing to grow in Apulia, and does not show any sign of slowing down. In May 2015, the pest was considered to be established and eradication no longer feasible. Since then, *Xylella Fastidiosa* issues have been regularly discussed with the relevant authorities in EU member countries in order to prevent its spreading to the neighbouring provinces of Taranto and Brindisi and to other Italian regions as well as to other EU countries. In this work, we focused on five olive orchard areas located in southern Italy (Fig. 1): Foggia, Matera, X2015, X2016 and X2017; the last three are located in Southern Apulia are infected by *Xylella Fastidiosa* in different periods from 2015 to 2017, while the first two are healthy. Our objective is to reveal the difference between the two types of areas (infected and not infected) by using the time series of MODIS ET at 500 m resolution with a sampling time of 8 days. The selected areas are featured by quite similar topographic (between flat and hilly) and climatic (mainly Mediterranean) conditions, which are quite relevant characteristics for the evapotranspiration dynamics that is the parameter analysed for the purpose or our investigation.

4. Methods

4.1. The Fisher–Shannon analysis

The Fisher–Shannon method is employed to investigate the informational properties of a time series that are the Fisher Information Measure (FIM) and Shannon entropy (SE); both quantify the properties of smoothness of the distribution of the series' values at local and global level, respectively. The FIM and SE are used to characterize the complexity of

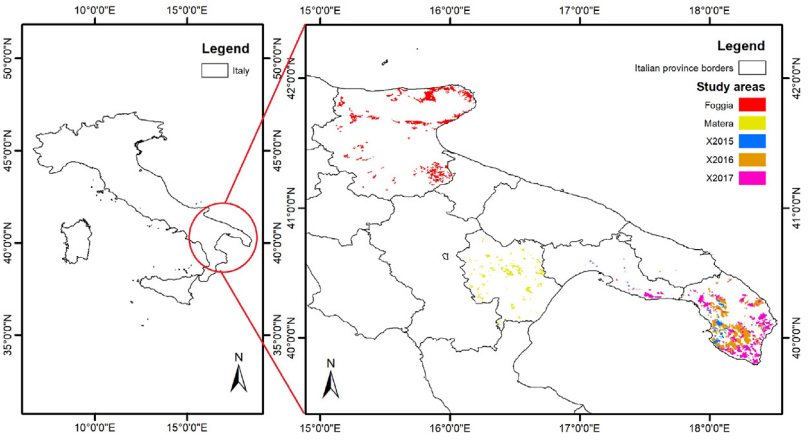

Fig. 1. Study areas.

non-stationary time series described in terms of order and organization the first [25], and uncertainty or disorder the second [26]. The FIM and SE are defined by the following formulae:

$$FIM = \int_{-\infty}^{+\infty} \left(\frac{\partial}{\partial x} f(x)\right)^2 \frac{dx}{f(x)} \tag{5}$$

$$SE = \int_{-\infty}^{+\infty} f_X(x) log(f_X(x)) dx \tag{6}$$

where $f(x)$ is the distribution of the series' values x. The Shannon entropy power N_X is generally used instead of SE:

$$N_X = \frac{1}{2\pi e} e^{2SE} \tag{7}$$

to deal always with positive quantities. FIM and N_X are not independent of each other due to the isoperimetric inequality $FIM \cdot N_X \geq D$ [44], where D is the dimension of the space, which is 1 for time series. In the so-called Fisher–Shannon Information plane (FSIP) that has FIM and N_X as coordinates, time series are represented by points that can occupy only the half-plane $FIM \cdot N_X \geq 1$, where the minimum $FIM \cdot N_X = 1$ is for Gaussian processes. The FSIP, which combines the global properties of the SEP and the local properties of FIM, is generally used to better discern time dynamics of time series [44].

4.2. The multifractal detrended fluctuation analysis

The multifractal detrended fluctuation analysis (MFDFA) [29] is an efficient method that is used to investigate particular properties of time series like heterogeneity, intermittency, different role played by small and large fluctuations, which define the multifractality of a series. If the series $x(i)$, for $i = 1, 2, \ldots, N$ has mean x_{ave}, the profile $y(i)$ is obtained by a simple integration:

$$y(i) = \sum_{k=1}^{i} [x(k) - x_{ave}] \tag{8}$$

The profile $y(i)$ is divided into $N_m = [N/m]$ contiguous boxes of identical size m that is called scale. In case N is not a multiple of m, since a short part of the series could remain at the end, the same procedure is applied from the end of the profile $y(i)$. In each of the $2N_m$ boxes the profile is fitted with a p-degree polynomial by a least square method, obtaining the following variance:

$$F^2(m, \nu) = \frac{1}{m} \sum_{i=1}^{m} \{[(\nu - 1)m + i] - y_\nu(i)\}^2, \nu = 1, \ldots, N_m \tag{9}$$

and

$$F^2(m, \nu) = \frac{1}{m} \sum_{i=1}^{m} \{[N - (\nu - N_m)m + i] - y_\nu(i)\}^2, \nu = N_m, \ldots, 2N_m \tag{10}$$

where $y_v(i)$ is the p-degree polynomial fitting the profile in the box v; the polynomial, thus, removes all the trends until the order p in the profile, and until the order p-1 in the original time series. Then, the qth order fluctuation function $F_q(m)$ is calculated as

$$F_q(m) = \{\frac{1}{2N_m}\sum_{v=1}^{2N_m}[F^2(m,v)]^{\frac{q}{2}}\}^{\frac{1}{q}} \tag{11}$$

where $q \neq 0$. For $q = 0$, $F_0(m)$ is calculated as follows:

$$e^{\frac{1}{4Nm}\sum_{v=1}^{2N_m} ln[F^2(m,v)]} \approx m^{h_o} \tag{12}$$

from which the exponent h_0 is obtained. For $q > 0$ the large fluctuations are enhanced, while for $q < 0$ the small ones are highlighted. The fluctuation function $F_q(m)$ increases with the box size or scale m; but if such increase is a power-law, then the series is characterized by long-range power-law correlations

$$F_q(m) \approx m^{h_q} \tag{13}$$

where h_q is called generalized Hurst exponent. If the exponent h_q is nearly constant with q, the series is called monofractal, indicating that the scaling behaviour of the small and large fluctuations is approximately identical. If the small and large fluctuations have different scaling behaviours, h_q decreases with q, indicating that more exponents are necessary to describe the fractality of the series that in this case is multifractal with a more complex structure. The range of the exponents h_q (h_q-range) is employed to quantify the multifractality of a series. The larger the h_q-range, the larger the multifractal degree of the series. The degree of multifractality can be investigated by means of the multifractal spectrum. From the following relationships (also known as the Legendre transform):

$$\tau(q) = qh_q - 1 \tag{14}$$

and

$$\alpha = \frac{d\tau}{dq} \tag{15}$$

the multifractal spectrum $f(\alpha)$ is calculated as:

$$f(\alpha) = q\alpha - \tau(q) \tag{16}$$

where α is the so-called Hölder exponent. The multifractal spectrum furnishes an indication of the relative dominance of the various scaling exponents in the series and is typically a single-humped shaped. It can be fitted by a second-degree polynomial:

$$f(\alpha) = \sum_{i=0}^{2} c_i(\alpha - \alpha_0)^i \tag{17}$$

where α_0 is the maximum. The width W of the multifractal spectrum is defined as:

$$W = \alpha_{max} - \alpha_{min} \tag{18}$$

where α_{max} and α_{min} are the two zeros of the fitted second-degree polynomial. W is often employed to quantify the multifractality in a series. The larger the value of W, the higher the multifractal degree of the series. The maximum α_0 of the multifractal spectrum conveys information about the regular behaviour of the process, and it is high for less regular processes with a finer structure, small for more regular ones.

4.3. The binomial multifractal model

Since the analysed pixel time series are rather short and present gap percentages up to 25% of the length of the series, we firstly checked the reliability of the MFDFA in detecting multifractal behaviour in short time series with gaps generated by the binomial multifractal model defined as follows. Given $0.5 < a < 1, N = 2^k, v = 1, \ldots, N$, the bi-nomial multifractal model is defined by:

$$x_v = a^{n(v-1)}(1-a)^{k-n(v-1)} \tag{19}$$

where $n(v)$ is the number of digits equal to 1 in the binary representation of the index v. The h_q of the binomial multifractal series can be theoretically calculated by the following formula [29]:

$$h_q = \frac{1}{q} - \frac{ln(a^q + (1-a)^q)}{qln(2)} \tag{20}$$

We generated a binomial multifractal series (with and without gaps) with a=0.75 and k=9. The length of the series is $N = 2^9 = 512$ that is comparable with the length of the analysed pixel time series. We applied the MFDFA with moment

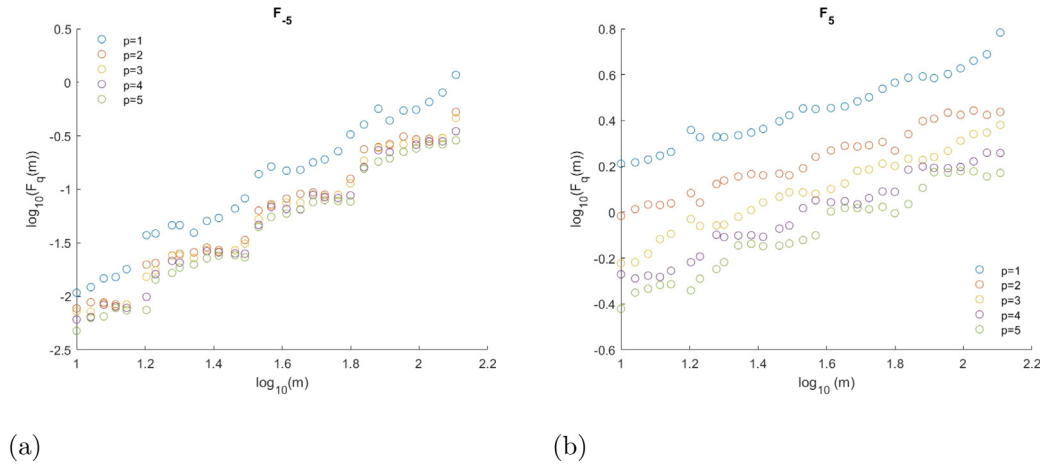

Fig. 2. Fluctuation function for $q = -5$ (a) and $q = 5$ (b) of the binomial series for different values of the degree of the detrending polynomial.

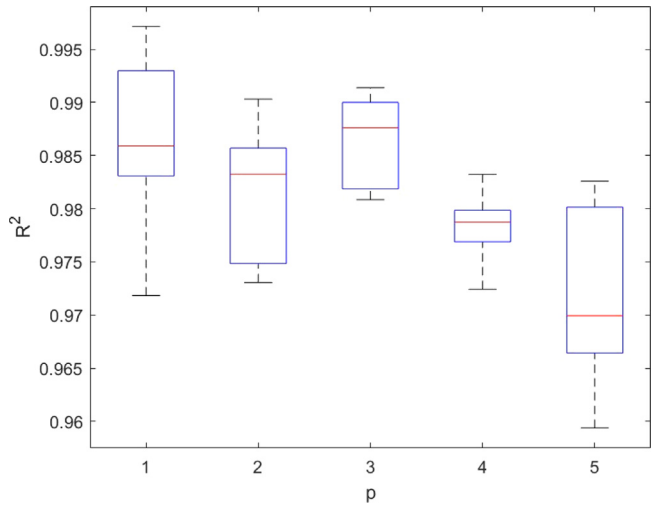

Fig. 3. Boxplot of R^2 of the binomial series for different values of the degree of the detrending polynomial.

order q ranging from -5 to 5, with a step of 0.5, the scale m from 10 to $\frac{1}{4}$ of the size of the series, and the detrending polynomial degree p from 1 to 5. Fig. 2 shows the comparison between the fluctuation function F_{-5} and F_5 varying the degree of the detrending polynomial. As it can be seen, different degrees of the detrending polynomial lead to different fluctuation functions for the same order q. Thus, the optimum degree of the detrending polynomial was chosen as that maximizing the coefficient of determination R^2 of the linear fit of the fluctuation function versus the scale m in log–log scales. Fig. 3 shows the boxplot of R^2 of the fluctuation functions for q ranging between -5 and 5 for different values of the degree p. An extensive study on the relationship between the multifractal parameters and the order of the detrending polynomial was performed by [45]. The choice of the optimum degree should be a trade-off between the average value of the coefficient of determination R^2 and its range. In our case, $p = 3$ can be considered the optimum degree of the detrending polynomial because the coefficient of determination R^2 ranges between 0.98 and 0.99 and has the largest average value. Thus, we calculated the generalized Hurst exponent h_q and the multifractal spectrum for $p = 3$. Fig. 4 shows $h_q \sim q$ and $f(\alpha) \sim \alpha$ for the theoretical case and the binomial series (for $p = 3$). Apart from the shift between the two spectra of the theoretical and the binomial series, the MFDFA seems able to detect multifractality in time series as short as the pixel time series analysed in this study. We investigated the performance of the MFDFA in detecting multifractal behaviour in binomial series affected by different percentages of missing data. We analysed five cases of gap percentages: 5%, 10%, 15%, 20% and 25% of the length of the series. For each case we generated 100 binomial series with missing data randomly placed within the series. For each series with gap we applied the MFDFA with q ranging from -5 to 5 and step of 0.5, scale m from 10 to $\frac{1}{4}$ of the size of the series, and the detrending polynomial degree $p = 3$. Before applying the MFDFA, the gap was removed stitching the two neighbours together. Fig. 5 shows the $\langle R^2 \rangle \sim q$ of the

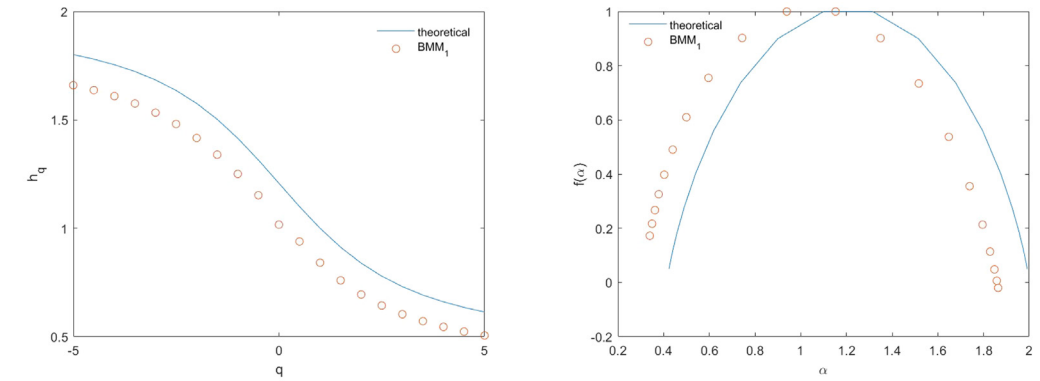

Fig. 4. $h_q \sim q$ (a) and $f(\alpha) \sim \alpha$ (b) for the theoretical (blue line) and binomial (red circles) series.

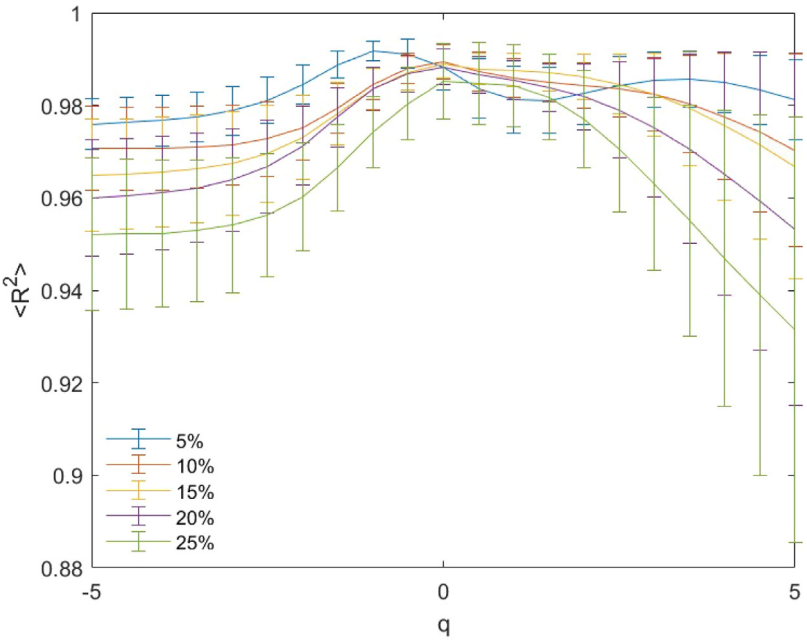

Fig. 5. Mean R^2 of the binomial series for different gap percentages.

linear fit of the fluctuation functions of the series for different gap percentages. Although the linear fit is better for series with lower gap percentage, nevertheless even for 25% of missing data the coefficient of determination remains reasonably high, indicating the good performance of MFDFA in detecting multifractality in short time series with gaps. Fig. 6 shows for different gap percentages the boxplot of multifractal width W, the range of h_q and the maximum of the multifractal spectrum α_0. The average values of each multifractal parameter calculated for the series with gaps is very close to that calculated for the series without gap, although the smaller the gap percentage the smaller the variability.

5. Results and discussion

For each area the number of analysed pixels is shown in Table 1. The percentage of missing data is less than 25% of the length of the series.

5.1. Spectral analysis

We firstly calculated the power spectrum of each pixel time series of the five investigated areas by means of the Periodogram analysis. Figs. 7 to 11 show the power spectrum, the heat map and the mean periodogram of the time series

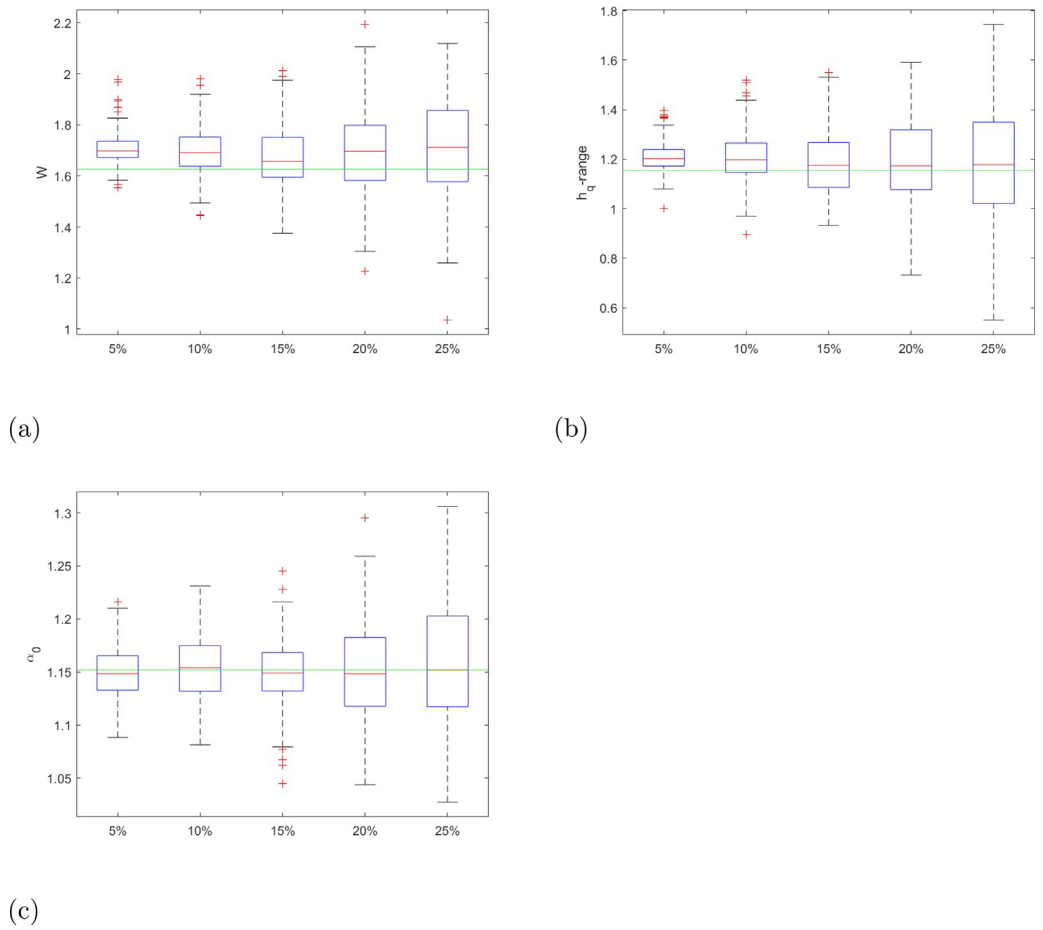

Fig. 6. Boxplot of multifractal width W (a), range of h_q (b) and maximum α_0 (c) for different gap percentages. The green horizontal line represents the value of the multifractal parameter calculated for the original binomial series without gaps.

Table 1
Number of analysed pixels for each investigated area.

Foggia	Matera	X2015	X2016	X2017
277	394	239	364	393

of the MODIS ET pixels for each area. The most powerful periodicities for almost all the pixels are the annual and sub-annual (6, 4 and 3 months) cycles; these represents the phenological cycles of vegetation that are very likely correlated with the meteo-climatic oscillations. Thus, in order to investigate the inner time dynamics of vegetation not influenced by these oscillations, we filtered them out. Fig. 12 shows, as an example, a pixel time series of Foggia area and its normalized residual after the spectral filtering.

5.2. Informational analysis

We applied the Fisher–Shannon analysis and calculated the FIM and the N_X for all the pixel time series of each investigated area. Fig. 13 shows the boxplots of the two informational quantities and the Fisher–Shannon Information Plane (FSIP) of $\langle FIM \rangle \sim \langle N_X \rangle$. Comparing the distribution of the FIM and SEP between infected and uninfected sites, we see that the distribution of these two parameters for the uninfected sites is characterized by a larger asymmetry than that of the infected sites, with the FIM (SEP) median larger (smaller) than that of the infected pixels. The FSIP shows a very clear discrimination between infected and uninfected sites. The infected sites are characterized by a larger SEP and a lower FIM, indicating a dominance of disorder or disorganization in the time dynamics of the satellite evapotranspiration data in comparison with the uninfected sites.

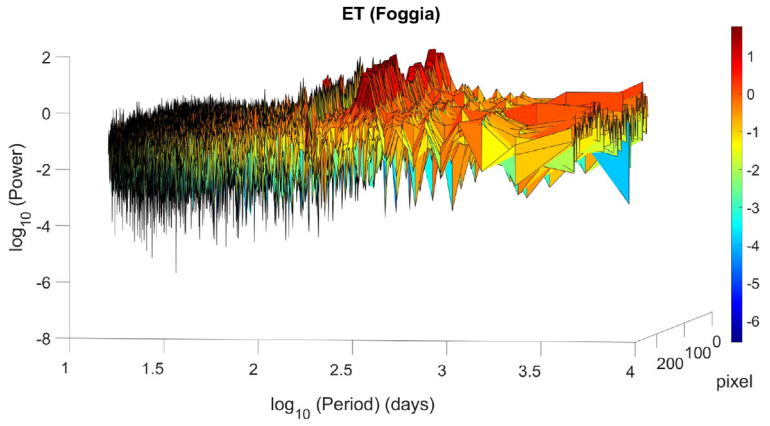

(a)

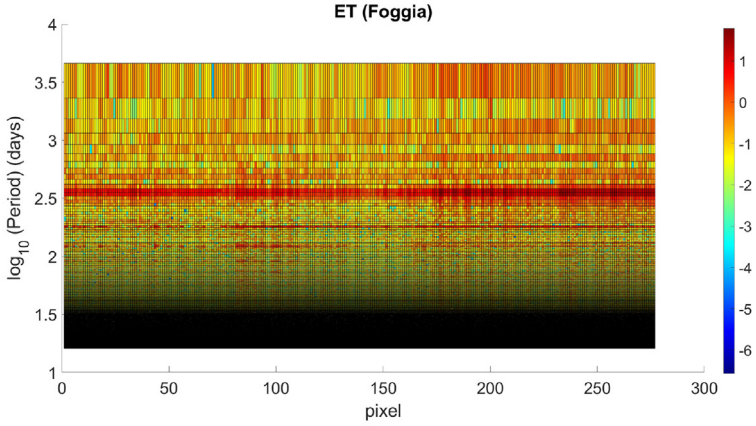

(b)

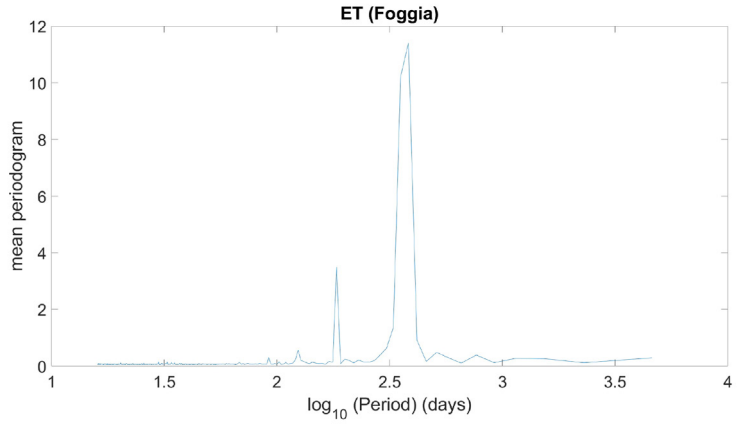

(c)

Fig. 7. (a) Power spectrum, (b) heat map and (c) mean periodogram of the time series of the MODIS ET pixels covering Foggia. (c) Mean periodogram.

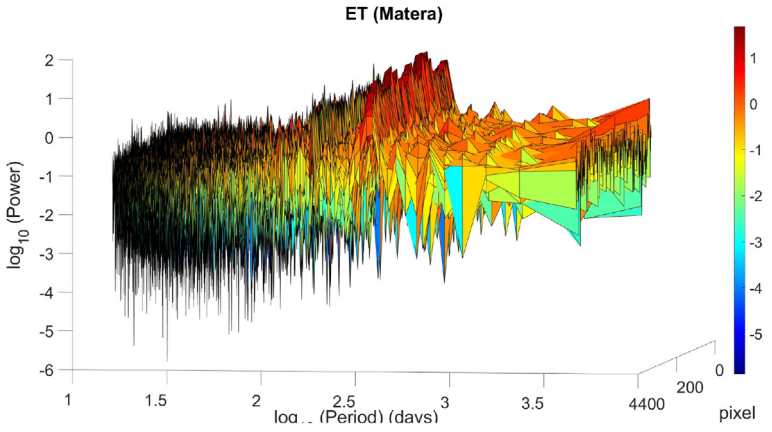

(a)

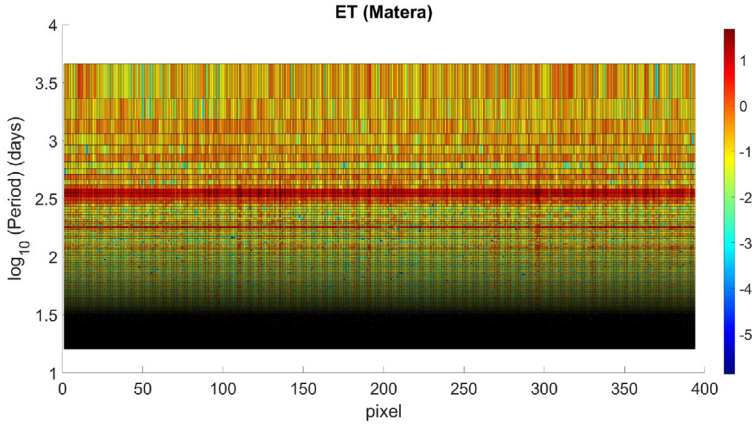

(b)

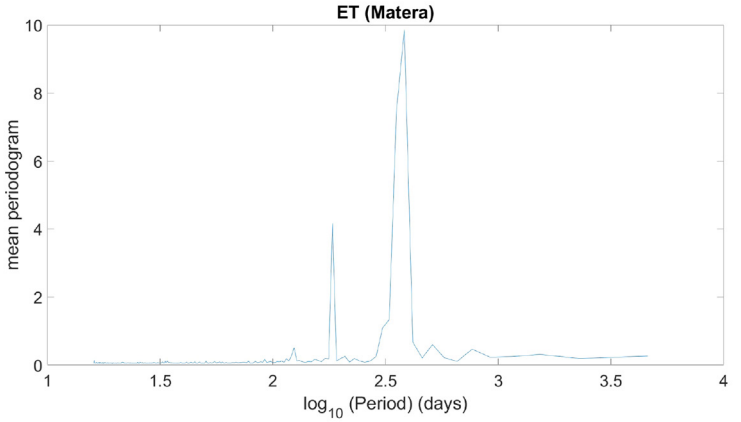

(c)

Fig. 8. (a) Power spectrum, (b) heat map and (c) mean periodogram of the time series of the MODIS ET pixels covering Matera.

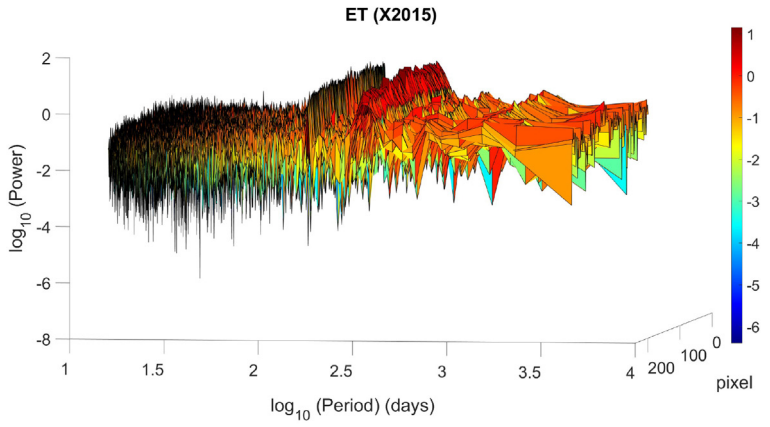

(a)

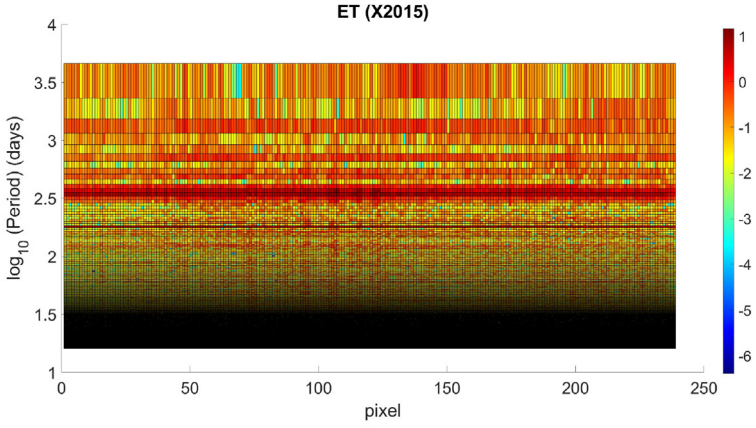

(b)

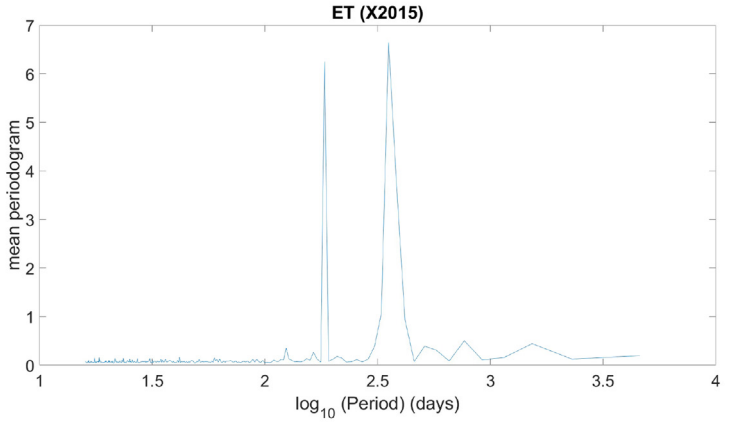

(c)

Fig. 9. (a) Power spectrum, (b) heat map and (c) mean periodogram of the time series of the MODIS ET pixels covering X2015.

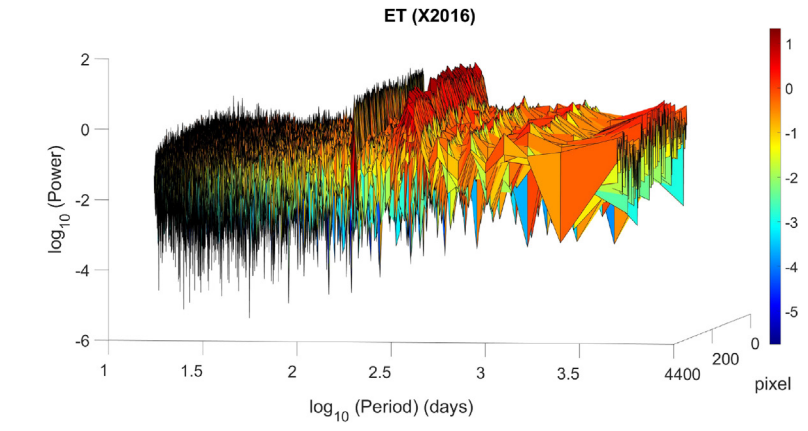

(a)

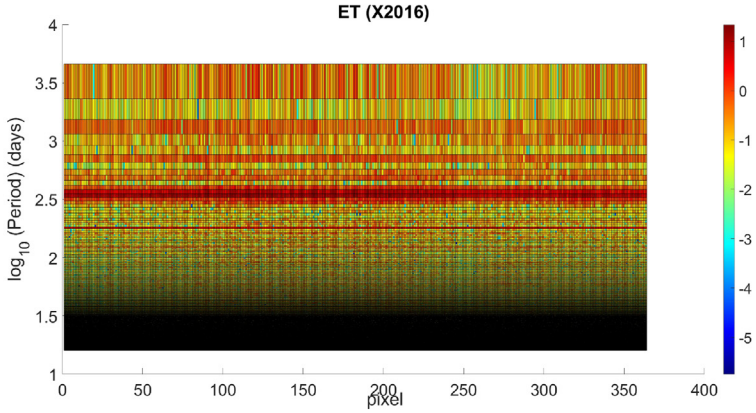

(b)

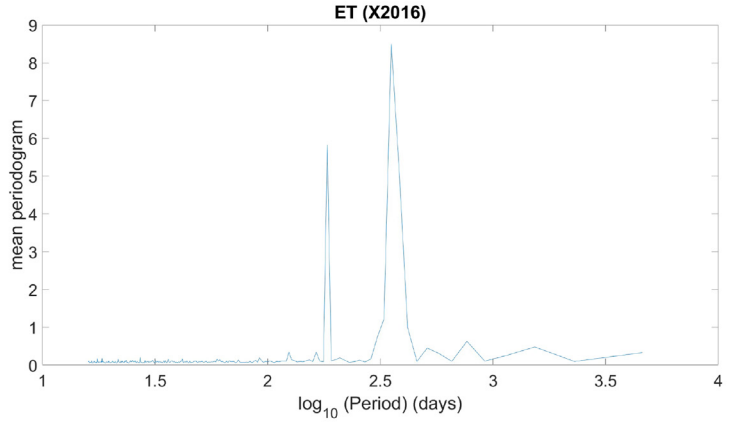

(c)

Fig. 10. (a) Power spectrum, (b) heat map and (c) mean periodogram of the time series of the MODIS ET pixels covering X2016.

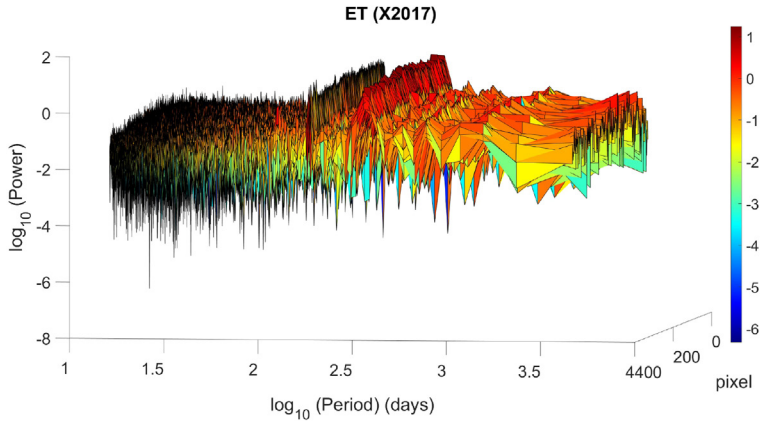

(a)

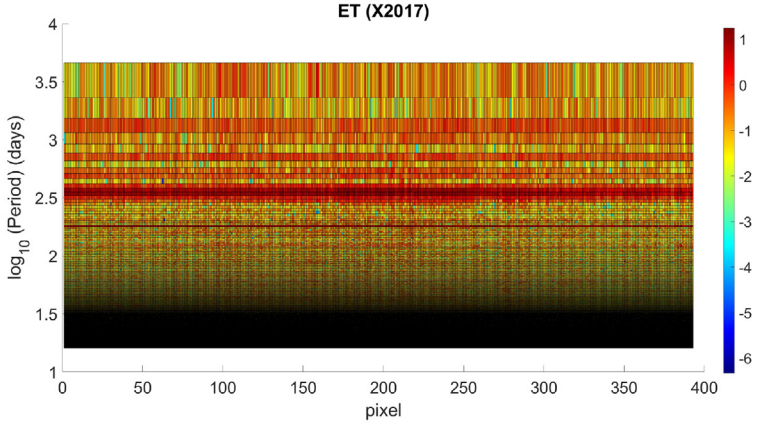

(b)

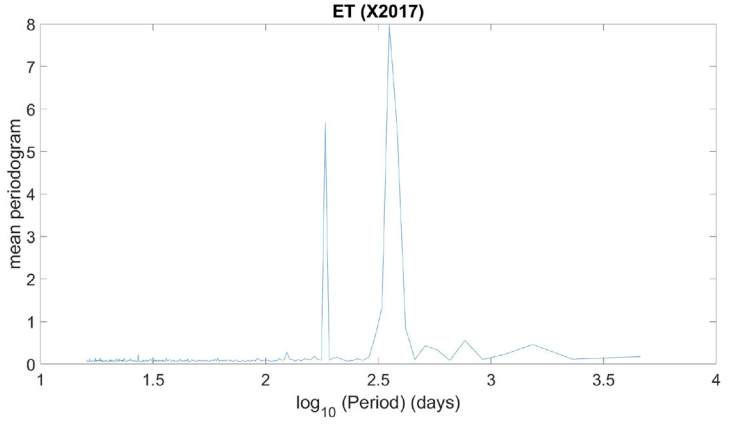

(c)

Fig. 11. (a) Power spectrum, (b) heat map and (c) mean periodogram of the time series of the MODIS ET pixels covering X2017.

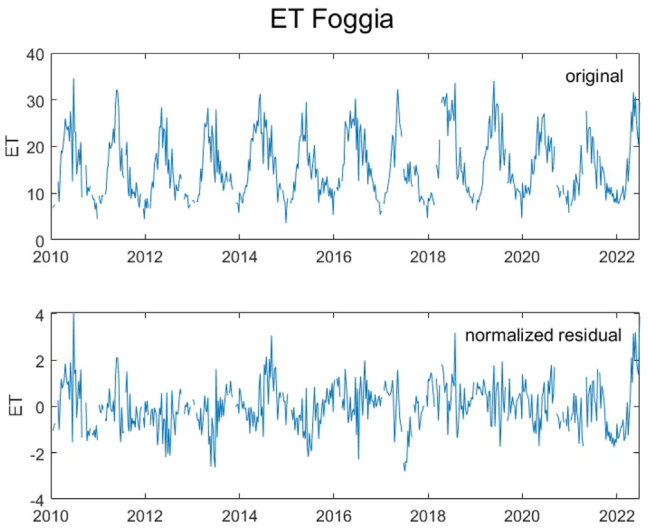

Fig. 12. Original and normalized residual time series of a MODIS ET pixel of Foggia dataset.

Table 2
Number of analysed pixels for each investigated area.

	Foggia	Matera	X2015	X2016	X2017
$< FIM >$	1.1822	1.1875	1.0865	1.0804	1.0756
$< SEP >$	0.9946	0.9953	1.0243	1.0283	1.0306
$< W >$	0.7168	0.7921	0.5166	0.5335	0.5150
$< h_q - range >$	0.2988	0.3595	0.1612	0.1705	0.1582
$< \alpha_0 >$	1.1718	1.2056	1.0223	1.0403	1.0570

5.3. Multifractal analysis

The length of the residual pixel time series is 575 and the maximum gap percentage is 25%. This gap percentage would not represent an issue, on the base of the results obtained for the binomial multifractal series shown in Section 2. We applied the MFDFA to each residual pixel time series, varying the moment order q from -5 to 5, the scale m from 10 to 1/4 of the length of the series. The gaps were eliminated by simply stitching together the two neighbours [46]. In order to select the optimum degree of the detrending polynomial, we calculated the fluctuation functions F_q for each q for detrending polynomial degree $p = 1, \ldots, 5$. For each F_q we computed the coefficient of determination R^2 of the linear fit of $log_{10}F_q \sim log_{10}(m)$. Fig. 14a shows, as an example, the distribution of R^2 for $p = 1$ of Foggia data; R^2 changes with the pixel and q. Fixing a threshold T for R^2, for instance $T = 0.9$, the distribution of R^2 becomes like in Fig. 13b. In order to be conservative, we analysed the multifractality of those pixels, whose $R^2 \geq T$ for any q, while those with $R^2 < T$ for at least one value of q were discarded. From here on, we fixed $T = 0.9$, and selected only those pixels with $R^2 \geq 0.9$. Fig. 15 shows the variation of $\langle R^2 \rangle_{pixel}$ (average of R^2 over all the selected pixels) versus q, for $p = 1, \ldots, 5$; we can see that $\langle R^2 \rangle_{pixel}$ is relatively larger for $p = 4$ for the areas not affected by *Xylella Fastidiosa* (Foggia and Matera), while it is the largest for $p = 3$ for the affected areas (X2015, X2016 and X2017). Thus, we analysed the multifractality with $p = 3$ and $p = 4$ for the *Xylella*-affected and *Xylella*-not affected areas, respectively. Moreover, with these values of p the number of selected pixels is 268/277 for Foggia, 387/388 for Matera, 238/238 for X2015, 362/362 for X2016 and 389/389 for X2017. Fig. 16 shows the boxplot of the multifractal parameters: h_q-range, W and α_0. Table 2 reports the means of the analysed parameters for each area.

5.4. Discussion

In this work we investigated the time variability of MODIS satellite ET of olive orchards in southern Italy to reveal the presence of one of the most dangerous phytobacteria, *Xylella Fastidiosa* that is greatly capable to provoke the death of a large amount of attacked trees by desiccation. For this reason, the time variation of MODIS ET satellite data was analysed to explore the time dynamics of the water status of plants; in fact, ET indirectly measures the loss of water content of vegetation and, thus, it is expected to be able to capture evidence of the presence of plant diseases induced by *Xylella Fastidiosa*. For all the investigated sites, both infected and healthy, the ET trend is featured by an oscillatory behaviour and represents the seasonal cycles of meteo-climatic origin. In particular, our analyses revealed two seasonal cycles: (1) an annual cycle that is quite similar for all the investigated sites; and (2) a six month seasonal cycle that is

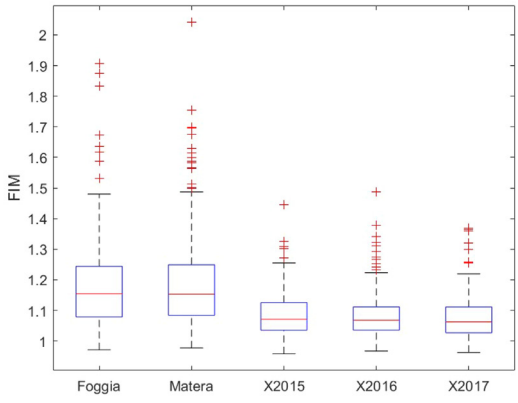

(a)

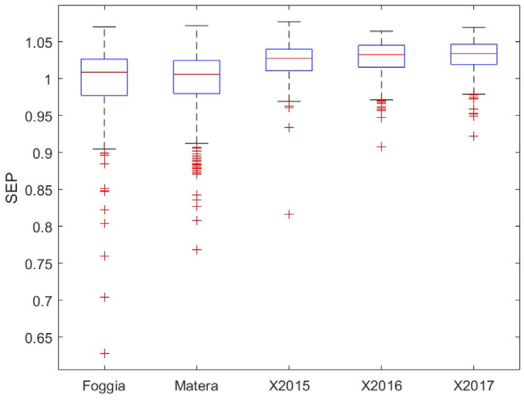

(b)

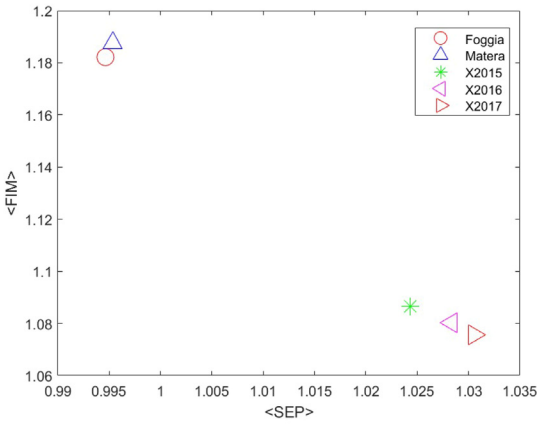

(c)

Fig. 13. Boxplot of FIM (a) and SEP (b). FSIP (c).

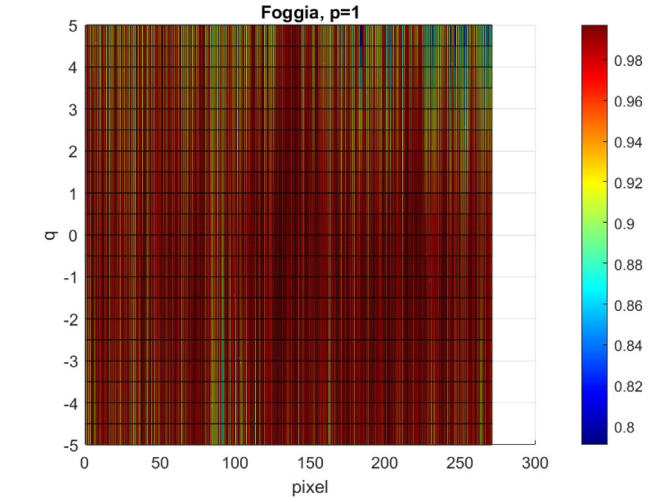

(a)

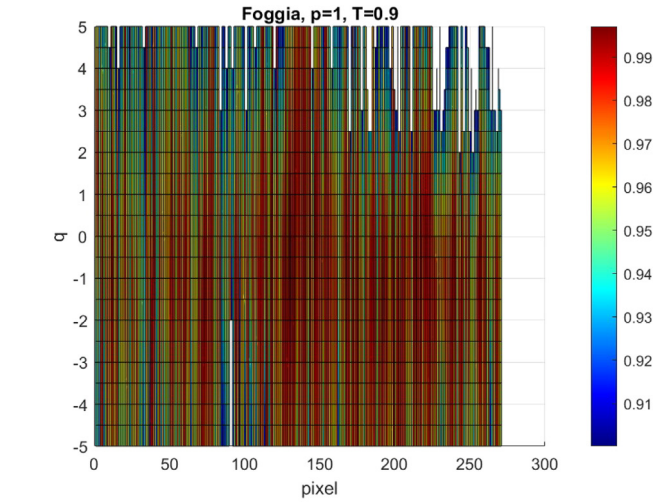

(b)

Fig. 14. R^2 of Foggia pixels for each q and p=1 without a threshold (a) and with the minimum threshold of 0.9 (b).

less pronounced for the healthy olive orchards and clearly enhanced for the those affected by bacterium. The more power observed at period of six months in the infected trees might be put in relationship with the semestral duration of the vector infectivity generally lasting from May to October, thus suggesting that the six month seasonal cycle is likely an evidence linked to the diseases induced by *Xylella Fastidiosa*.

In our study, the ET time series of infected sites are characterized by a larger SEP and lower FIM indicating that their time dynamics appear more disordered (less organized) than that of sites not infected by *Xylella Fastidiosa*. FIM and SEP relate to the local and global properties of the distribution of a time series, respectively. Thus, the larger SEP shown by the ET of infected sites could indicate a dominance of the global variations of their distribution larger than that shown by the ET of not infected sites, whose distribution, in contrast, is governed by the local variations. The different informational response of the ET of infected and not infected sites could be linked to the different nutritional processes that are largely damaged or even annihilated in infected olive trees. The nutritional system of olive trees is governed by mechanisms that control water and nutrient fluxes through vessels of the xylem from the roots to the stem and up to the leaves. In healthy trees this system is complex and undergoes several different processes that involve interactions with the environment. A healthy tree is capable to respond more effectively to the local environmental factors; this larger resilience is reflected in a larger heterogeneity, well depicted by a larger FIM and lower SEP. Such larger heterogeneity and complexity are also indicated by the higher h_q-range, multifractal width W and α_0; these three parameters quantify

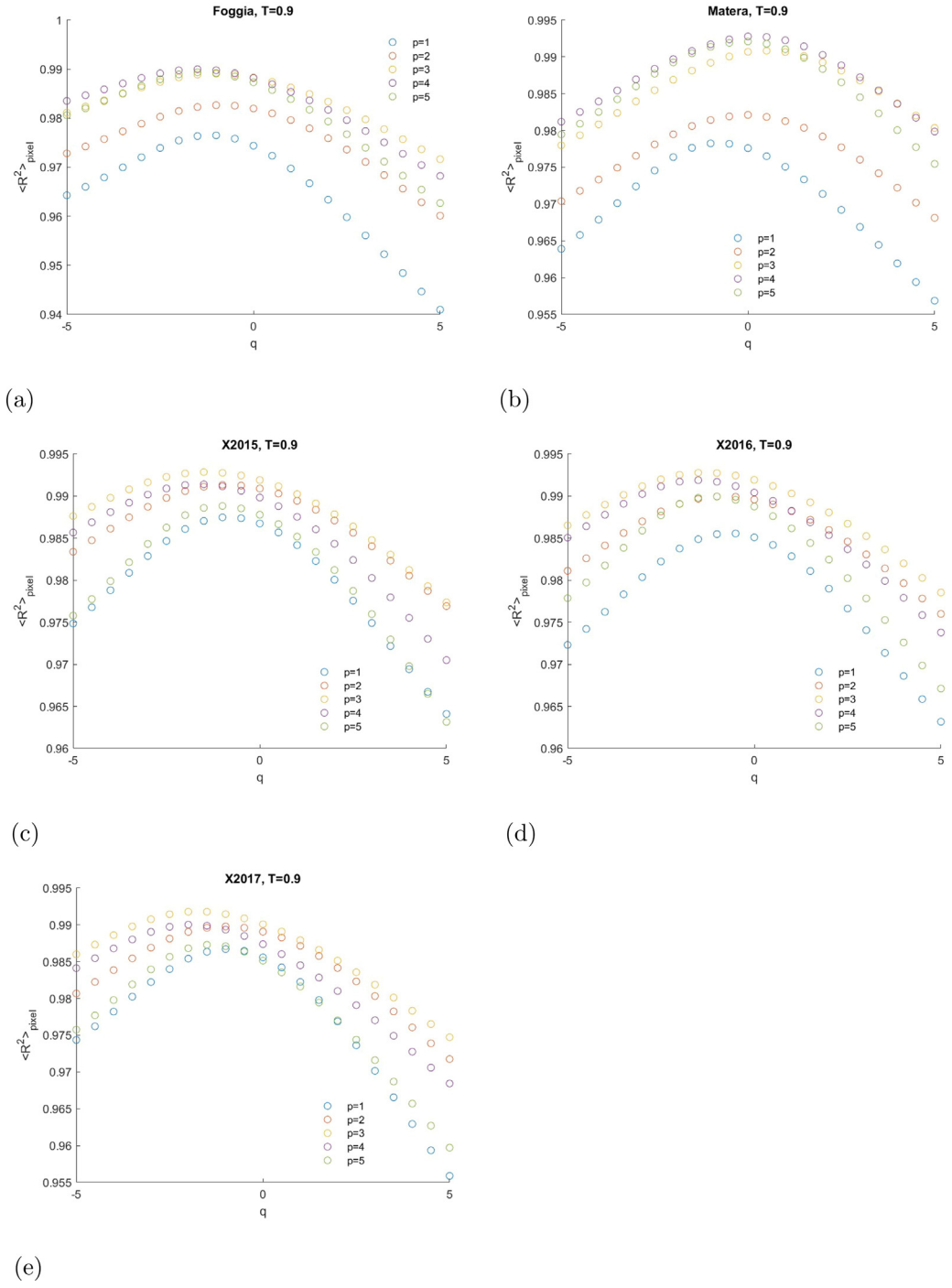

Fig. 15. Mean $R^2_{pixel} \sim q$ for Foggia (a), Matera (b), X2015 (c), X2016 (d) and X2017 (e).

the multifractality of a series. The h_q-range and the width W play similar role, since they quantify the variety of the scaling exponents of the series; thus relatively large h_q-range and width W suggest that the series showcases a relatively irregular behaviour characterized by a multitude of scaling exponents that make it to be different from a series with a nearly regular behaviour with homogeneous variations characterized, instead, by smaller h_q-range and width W. The α_0 parameter gives information on the structure of the ET series, being larger for less regular processes with a finer structure; if the process becomes more regular it loses its fine structure, and α_0 becomes smaller. The larger homogeneity of the ET

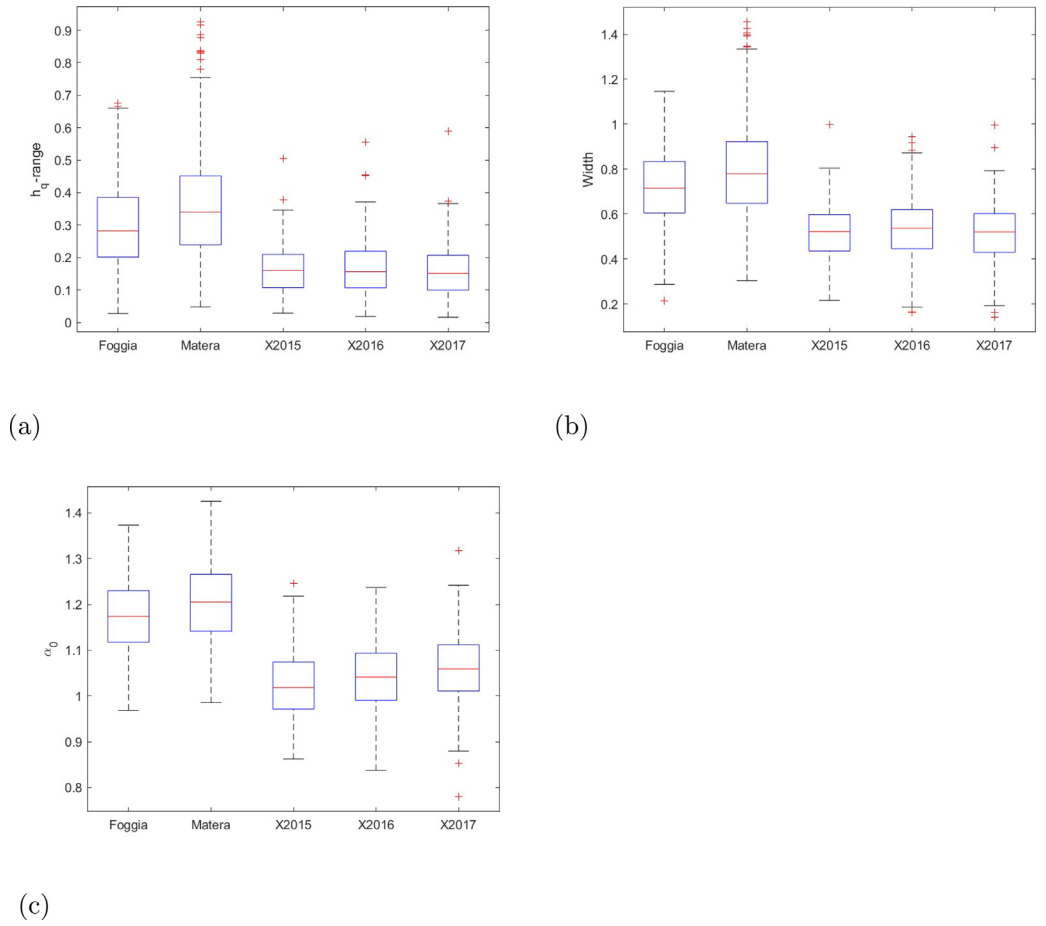

Fig. 16. Boxplot of h_q-range (a), width (b) and (c) α_0 of the investigated areas.

of the infected trees indicates such more regular behaviour that, moreover, reveals a less resilience to local environmental perturbations, due to the status of desiccation induced by *Xylella Fastidiosa*, which reflects the inefficiency of the nutritional control mechanisms associated with the disease. The multifractality quantifies also the degree of nonlinearity [41] in the mechanisms governing the ET series. For infected trees the ET series have the same scaling behaviour regardless of the external driving forces; while, healthy trees are characterized by nonlinear processes that generate ET series with different scaling properties that would depend on the external driving conditions and make them to have a better resilient behaviour. The findings of this study strengthen the results found in [47], where the investigation by MDFDFA and FS methods was performed at a global scale considering just two populations of pixels (infected and uninfected) and the classification performance evaluated by using the ROC analysis. In the present study, the analysis took into account also the area, since the pixels are analysed for two uninfected areas and three infected areas. Although the general meteo-climatic and topographical conditions of all the investigated areas are similar, being characterized by Mediterranean climate and flat to hilly terrain, at a regional/local scale climatic and morphological differences could arise among the areas. Furthermore, in Italy the measures to detect and contrast Xylella are established at a regional level, which means that they could be different from one region to another. Thus, in this study we found that at a local scale (at the level of area) the MFDFA and FS perform satisfactorily as well as at a global scale in discriminating between infected and uninfected pixels.

6. Conclusions

The aim of the present work was to detect signs of *Xylella Fastidiosa* in olive groves in Southern Italy. For this purpose, we analysed the time series of pixels of MODIS satellite evapotranspiration covering five areas, among which two (Foggia and Matera) are healthy and three (X2015, X2016 and X2017) are infected. The evapotranspiration is used to monitor the water status of olive orchards; thus, it resulted well suited to reveal possible sign of the disease caused by *Xylella Fastidiosa* whose main effect is the rapid branch desiccation. In order to remove the seasonal variability, we firstly filtered

out from the time series the annual and sub-annual cycles, and the detrended series were, then, analysed by the Fisher–Shannon analysis and the multifractal detrended fluctuation analysis. Our findings point out to a clear discrimination of the informational and the multifractal parameters between healthy and infected trees. These results could contribute to the definition of an operational tool for early diagnosis of *Xylella Fastidiosa* infection, based on multiscale, multisensor, multitemporal monitoring of biophysical parameters related to the state of vegetation.

CRediT authorship contribution statement

Luciano Telesca: Conceptualization, Methodology, Formal analysis, Investigation, Writing – original draft, Writing – review & editing, Visualization. **Nicodemo Abate:** Data curation. **Farid Faridani:** Data curation. **Michele Lovallo:** Software. **Rosa Lasaponara:** Conceptualization, Investigation, Resources, Writing – review & editing, Project administration, Funding acquisition.

Declaration of competing interest

The authors declare the following financial interests/personal relationships which may be considered as potential competing interests: The authors declare that they have no known competing financial interests or personal relationships that could have appeared to influence the work reported in this paper.

Data availability

Data will be made available on request.

Acknowledgement

This work was supported by the project COELUM funded by CNR, Italy.

References

[1] P. Wallingford, T. Morelli, J. Allen, E. Beaury, D. Blumenthal, B. Bradley, J. Dukes, R. Early, E. Fusco, D. Goldberg, I. Ibàñez, B. Laginhas, M. Vilà, C. Sorte, Adjusting the lens of invasion biology to focus on the impacts of climate-driven range shifts, Nat. Clim. Chang. 10 (2020) 398–405.
[2] P. Pyšek, P. Hulme, D. Simberloff, S. Bacher, T. Blackburn, J. Carlton, W. Dawson, F. Essl, L. Foxcroft, P. Genovesi, J. Jeschke, I. Kühn, A. Liebhold, N. Mandrak, L. Meyerson, A. Pauchard, J. Pergl, H. Roy, H. Seebens, M. Kleunen, M. Vilà, M.W. eld, D. Richardson, Scientists warning on invasive alien species, Biol. Rev. 95 (2020) 1511–1534.
[3] T. Chaloner, S. Gurr, D. Bebber, Plant pathogen infection risk tracks global crop yields under climate change, Nat. Clim. Chang. 11 (2021) 710–715.
[4] J. Sorensen, R. Gill, A range extension of homalodisca coagulata (say) (Hemiptera: Clypeorrhyncha: Cicadellidae) to Southern California, Pan-Pac. Entomol. 72 (1996) 160–161.
[5] J. Janse, A. Obradovic, Xylella fastidiosa: its biology, diagnosis, control and risks, J. Plant Pathol. 92 (2010) S35–S48.
[6] K. Schneider, W. van der Werf, M. Cendoya, M. Mourits, J. Navas-Cortés, A. Vicent, A. Oude Lansink, Impact of xylella fastidiosa subspecies pauca in European olives, Proc. Natl. Acad. Sci. USA 117 (2020) 9250–9259.
[7] S. Hearon, J. Sherald, S. Kostka, Association of xylem-limited bacteria with elm, sycamore, and oak leaf scorch, Can. J. Bot. 58 (1980) 1986–1993.
[8] J. Wells, Isolation, culture, and pathogenicity of the bacterium causing phony disease of peach, Phytopathology 73 (1980) 859.
[9] M. Saponari, D. Boscia, F. Nigro, G. Martelli, Identification of DNA sequences related to xylella fastidiosa in oleander, almond and olive trees exhibiting leaf scorch symptoms in Apulia (Southern Italy), J. Plant Pathol. 95 (2013) 668.
[10] N. Amanifar, M. Taghavi, K. Izadpanah, G. Babaei, Isolation and pathogenicity of Xylella fastidiosa from grapevine and almond in Iran, Phytopathol. Mediterr. (2014) 318–327.
[11] L. Leu, C. Su, Isolation, cultivation, and pathogenicity of xylella fastidiosa, the causal bacterium of pear leaf scorch disease in Taiwan, Plant Dis. 77 (1993) 642–646.
[12] M. Jeger, D. Caffier, T. Candresse, E. Chatzivassiliou, K. Dehnen-Schmutz, G. Gilioli, J.-C. Grégoire, J. Jaques Miret, A. MacLeod, M. Navajas Navarro, B. Niere, S. Parnell, R. Potting, T. Rafoss, V. Rossi, G. Urek, A. Van Bruggen, W. Van der Werf, J. West, S. Winter, R. Almeida, D. Bosco, M.-A. Jacques, B. Landa, A. Purcell, M. Saponari, E. Czwienczek, A. Delbianco, G. Stancanelli, C. Bragard, Scientific opinion on the updated pest categorisation of Xylella fastidiosa, EFSA J. 16 (2018) 5357.
[13] R. Krugner, M.S. Sisterson, J. Chen, D.C. Stenger, M.W. Johnson, Evaluation of olive as a host of Xylella fastidiosa and associated sharpshooter vectors, Plant Dis. 99 (2014) 1186–1193.
[14] R.M. Haelterman, P.A. Tolocka, M.E. Roca, F.A. Guzmán, F.D. Fernández, M.L. Otero, First presumed diagnosis of Xylella fastidiosa causing olive scorch in Argentina, J. Plant Pathol. 97 (2015) 393.
[15] H.D. Coletta-Filho, C.S. Francisco, J.R.S. Lopes, A.F. De Oliveira, L.F.O. Da Silva, First report of olive leaf scorch in Brazil, associated with Xylella fastidiosa subsp. pauca, Phytopathol. Mediterr. 55 (2016) 130–135.
[16] A. Giampetruzzi, M. Chiumenti, M. Saponari, G. Donvito, A. Italiano, G. Loconsole, D. Boscia, C. Cariddi, G.P. Martelli, P. Saldarelli, Draf genome sequence of Xylella fastidiosa CoDiRO strain, Genome Announc. 3 (2015) e01538–14.
[17] G. Strona, C.C. J., P. Beck, Network analysis reveals why Xylella fastidiosa will persist in Europe, Sci. Rep. 7 (2017) 71.
[18] S. Yoon, W.-L. Lee, Spatial analysis of climatic and dispersion characteristics of Xylella fastidiosa outbreak by insect vectors, J. Asia-Pac. Entomol. 26 (2023) 102011.
[19] M. Godefroid, N. Meurisse, F. Groenen, C. Kerdelhué, J.-P. Rossi, Current and future distribution of the invasive oak processionary moth, Biol. Invasions 22 (2020) 523–534.
[20] C. Bock, G. Poole, P. Parker, T. Gottwald, Plant disease severity estimated visually, by digital photography and image analysis, and by hyperspectral imaging, CRC. Crit. Rev. Plant Sci. 29 (2010) 59–107.

[21] A. Castrignanó, A. Belmonte, I. Antelmi, R. Quarto, F. Quarto, S. Shaddad, V. Sion, M.R. Muolo, N.A. Ranieri, G. Gadaleta, E. Bartoccetti, C. Riefolo, S. Ruggieri, F. Nigro, Semi-automatic method for early detection of xylella fastidiosa in olive trees using UAV multispectral imagery and geostatistical-discriminant analysis, Remote Sens. 13 (2021) 14.
[22] P. Zarco-Tejada, C. Camino, P. Beck, R. Calderon, A. Hornero, R. Hernández-Clemente, T. Kattenborn, M. Montes-Borrego, L. Susca, M. Morelli, V. Gonzalez-Dugo, P.R.J. North, B.B. Landa, D. Boscia, M. Saponari, J.A. Navas-Cortes, Previsual symptoms of Xylella fastidiosa infection revealed in spectral planttrait alterations, Nat. Plants 4 (2018) 432–439.
[23] C. Camino, R. Calderón, S. Parnell, H. Dierkes, Y. Chemin, M. Román-Écija, M. Montes-Borrego, B.B. Landa, J.A. Navas-Cortes, P.J. Zarco-Tejada, B. P.S.A., Detection of *Xylella fastidiosa* in almond orchards by synergic use of an epidemic spread model and remotely sensed plant traits, Remote Sens. Environ. 260 (2021) 112420.
[24] M. Saponari, A. Giampetruzzi, G. Loconsole, D. Boscia, P. Saldarelli, Xylella fastidiosa in Olive in Apulia: Where we stand, Phytopathology 109 (2019) 175–186.
[25] B.R. Frieden, Fisher information, disorder, and the equilibrium distributions of physics, Phys. Rev. A 41 (1990) 4265–4276.
[26] V.V. Kharin, F.V. Zwiers, On the ROC score of probability forecasts, J. Climate 16 (2013) 4145–4150.
[27] L.H. Fernandes, F.H. de Araujo, I.E. Silva, J.S. Neto, Macroeconophysics indicator of economic efficiency, Physica A 573 (2021) 125946.
[28] L.H.S. Fernandes, F.H.A. de Araujo, M.A.R. Silva, B. Acioli-Santos, Predictability of COVID-19 worldwide lethality using permutation-information theory quantifiers, Results Phys. 26 (2021) 104306.
[29] J.W. Kantelhardt, S.A. Zschiegner, E. Konscienly-Bunde, S. Havlin, A. Bunde, H.E. Stanley, Multifractal detrended fluctuation analysis of nonstationary time series, Physica A 316 (2002) 87–114.
[30] L.H.S. Fernandes, M.A.R. Silva, F.H.A. de Araujo, Anti-persistent adherence dynamic of the COVID-19 vaccines, Phys. Scr. 98 (2022) 015017.
[31] J.K. Ochab, M. Watorek, A. Ceglarek, M. Fafrowicz, K. Lewandowska, T. Marek, B. Sikora-Wachowicz, P. Oświęcimka, Task-dependent fractal patterns of information processing in working memory, Sci. Rep. 12 (2022) 17866.
[32] Y.-W. Zhou, J.-L. Liu, Z.-G. Yu, Z.-Q. Zhao, V. Anh, Fractal and complex network analyses of protein molecular dynamics, Physica A 416 (2014) 21–32.
[33] Q. Cheng, X. Liu, X. Zhu, Cryptocurrency momentum effect: DFA and MF-DFA analysis, Physica A 526 (2019) 120847.
[34] A. Chamoli, R. Yadav, Multifractality in seismic sequences of NW himalaya, Nat. Hazards 77 (2015) 19–32.
[35] D. Dwivedi, A. Chamoli, S.K. Rana, Wavelet entropy: A new tool for edge detection of potential field data, Entropy 25 (2023) 240.
[36] A.S.A. da Silva, R.S.C. Menezes, L. Telesca, B. Stosic, T. Stosic, Fisher-Shannon analysis of drought/wetness episodes along a rainfall gradient in Northeast Brazil, J. Climatol. 41 (2021) E2097–E2110.
[37] F. Guignard, D. Mauree, M. Lovallo, M. Kanevski, L. Telesca, Fisher–Shannon complexity analysis of high-frequency urban wind speed time series, Entropy 21 (2019) 47.
[38] S. Tripaldi, M. Telesca, Spectral and informational analysis of temperature and chemical composition of solfatara fumaroles (campi flegrei, Italy), Entropy 23 (2021) 593.
[39] S. Tripaldi, M. Lovallo, M. Filippucci, L. Telesca, Space-time analysis of informational properties of GPS time series recorded at the campi flegrei caldera (Italy), J. Volcanol. Geotherma Res. 433 (2023) 107734.
[40] R. Ba, M. Lovallo, W. Song, H. Zhang, L. Telesca, Multifractal analysis of MODIS aqua and terra satellite time series of normalized difference vegetation index and enhanced vegetation index of sites affected by wildfires, Entropy 24 (2022) 1748.
[41] P. Ivanov, L. Amaral, A. Goldberger, S. Havlin, M.G. Rosenblum, Z.R. Struzik, H.E. Stanley, Multifractality in human heartbeat dynamics, Nature 399 (1999) 461–465.
[42] Q. Mu, M. Zhao, S.W. Running, Improvements to a MODIS global terrestrial evapotranspiration algorithm, Remote Sens. Environ. 115 (2011) 1781–1800.
[43] L. Laipelt, R.H.B. Kayser, A.S. Fleischmann, A. Ruhoff, W. Bastiaanssen, T.A. Erickson, F. Melton, Long-term monitoring of evapotranspiration using the SEBAL algorithm and google earth engine cloud computing ISPRS, J. Photogram. Remote Sens. 178 (2021) 81–96.
[44] M. Martin, J. Perez, A. Plastino, Fisher information and nonlinear dynamics, Physica A 291 (2001) 523–532.
[45] P. Oświęcimka, Drożdż, J. Kwapień, A.Z. Górski, Effect of detrending on multifractal characteristics, Acta Phys. Pol. A 123 (2013) 597–603.
[46] Z. Chen, P.C. Ivanov, K. Hu, H.E. Stanley, Effect of nonstationarities on detrended fluctuation analysis, Phys. Rev. E 65 (2002) 041107.
[47] L. Telesca, N. Abate, F. Faridani, M. Lovallo, R. Lasaponara, Discerning xylella fastidiosa-infected olive orchards in the time series of MODIS terra satellite evapotranspiration data by using the Fisher–Shannon analysis and the multifractal detrended fluctuation analysis, Fractal Fract. 7 (2023) 466.